Prediction of Porosity and Permeability of Caved Zone in Longwall Gobs

C. Özgen Karacan

Abstract The porosity and permeability of the caved zone (gob) in a longwall operation impact many ventilation and methane control related issues, such as air leakage into the gob, the onset of spontaneous combustion, methane and air flow patterns in the gob, and the interaction of gob gas ventholes with the mining environment. Despite its importance, the gob is typically inaccessible for performing direct measurements of porosity and permeability. Thus, there has always been debate on the likely values of porosity and permeability of the caved zone and how these values can be predicted. This study demonstrates a predictive approach that combines fractal scaling in porous medium with principles of fluid flow. The approach allows the calculation of porosity and permeability from the size distribution of broken rock material in the gob, which can be determined from image analyzes of gob material using the theories on a completely fragmented porous medium. The virtual fragmented fractal porous medium so generated is exposed to various uniaxial stresses to simulate gob compaction and porosity and permeability changes during this process. The results suggest that the gob porosity and permeability values can be predicted by this approach and the presented models are capable to produce values close to values documented by other researchers.

List of Symbols

A_G Area of grains, L^2
A_P Area of pores, L^2
A_T Total area, L^2
D_F Fragmentation fractal dimension (fractal dimension)
D_P Pore-area fractal dimension (fractal dimension)
D_T Tortuosity fractal dimension (fractal dimension)

C. Ö. Karacan
NIOSH, Pittsburgh Research Laboratory, Pittsburgh, PA 15236, USA
e-mail: cok6@cdc.gov

f	Fracturing probability term (dimensionless)
h	Thickness of the analysis location, L
k	Permeability, L^2
L_t	Tortuous length, L
L_o	Representative length, L
s	Number of virtual pore-size fractions, number, N
N_i	Number of particles in the ith size class, number, N
ΔP	Differential pressure, P
r	Similarity coefficient (dimensionless)
m	Weibull modulus (dimensionless)
Q	Total flow rate, L^3/t
V	Volume of porous medium, L^3
α	Shape factor in H–P equation
η	Pore diameter, L
η_i	Pore diameter of the ith size class, L
ϕ	Porosity of fragmented porous medium, $L_p^3 L_b^{-3}$
ϕ_i	Porosity in partial volume in fractal porous media, $L_p^3 L_b^{-3}$
ϕ_T	Total porosity, $L_p^3 L_b^{-3}$, dimensionless
Γ	Pore coefficient, dimensionless
μ	Viscosity, $ML^{-1}t^{-1}$
Ω_i	Particle diameter of the ith size class, L
$\bar{\Omega}$	Average particle diameter, L
Π	Hydraulic resistance, L^{-2}
Ψ	Arbitrary cross-sectional area, L^2
Λ	Plastic compressibility index (dimensionless)
$v(x, y)$	Fluid velocity perpendicular to x–y-plane, L/t
ε	Surface energy in linear-elastic fracture mechanics, E
σ_0	Tensile strength of the grains, P
$\bar{\sigma}$	Applied macroscopic stress, P
Permeability conversion factor	1 Darcy $= 10^{-12} m^2 = 10^{-8} cm^2$

1 Introduction

Longwall mining is an underground mining method that can maximize coal production in coal beds, which contain few geological discontinuities. In these operations, a mechanical shearer progressively mines a large block of coal, called a panel, which is outlined with development entries or gate roads. As the coal is extracted, the supports automatically advance and the roof strata allowed to cave behind the supports (Karacan et al. 2007) creating large-scale disturbances of the surrounding rock mass due to fracturing and caving of mine roof behind the shields. The caved zone (gob) created by longwall mining could reach 4–11 times the thickness of the mining height where overburden rocks are weak and porous. The gob material is highly fragmented and is broken into irregular shapes of various sizes. The gob can contain high void ratios due to fragmented rock pieces and may provide high permeability flow paths for any fluid within the zone or flowing from surrounding formations into the mining environment. Figure 1 shows example pictures from the caved zones of two Eastern Kentucky coal mines.

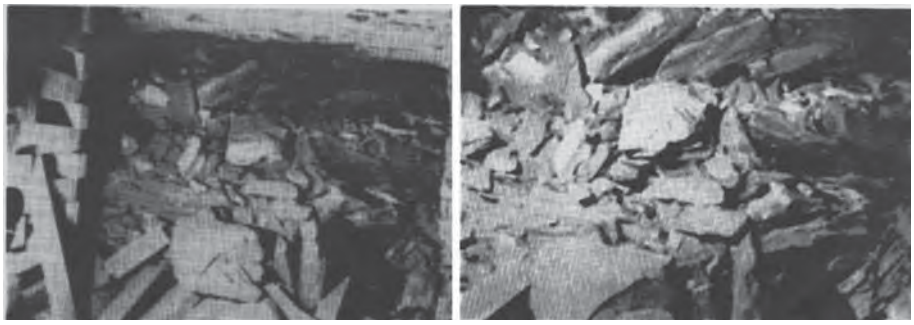

Fig. 1 Gob materials photographed in two Eastern Kentucky coal mines (from Pappas and Mark 1993)

As mining progresses, the gob gradually consolidates sufficiently to support large loads resulting from the overburden weight (Pappas and Mark 1993). Consolidation results in a reduction in the void ratio (porosity) and the associated permeability. Although reduced to some degree due to compaction, prevailing high permeability pathways in the gob still affect the leakage of ventilation airflow from the face into the gob, the flow of methane from surrounding sources into the gob and into the mine, and the performance of methane extraction gob gas ventholes. Thus, an understanding of compaction phenomena and the resultant reservoir properties of gob material is very important for developing adequate methane control strategies.

Accuracy of models for predicting methane flow in the vicinity of the longwall face and methane control in longwall mines depends on an accurate representation of the gob porosity and permeability. Despite the importance of these two reservoir properties, their predictions are difficult have been conducted by only a few studies (Brunner 1985; Ren et al. 1997; Wendt and Balusu 2002; Esterhuizen and Karacan 2005, 2007; Whittles et al. 2006; Karacan et al. 2007). This may be due to challenges and unknowns related to the gob environment. These challenges are even more difficult due to the inaccessibility of the gob environment for conducting direct measurements of porosity and permeability using conventional tests.

This work presents a fractal porous medium model to predict gob porosity and permeability for controlling methane flow and to predict air leakage into the gob. For this approach, the particle size data for simulated gob material given by Pappas and Mark (1993) were used to calculate fragmentation fractal dimensions and particle size distributions before and after controlled loading tests. The size distributions were scaled up to real dimensions to describe the geometry and size of flow channels. Fractal geometry concepts were used to construct porosity and flow equations for a completely fragmented porous medium through fragmentation, tortuosity, and area fractal dimensions (Karacan and Halleck 2003). The fragmented fractal porous medium model was exposed to various uniaxial compressive stresses to simulate gob compaction and to predict porosity–permeability changes in the gob due to loading.

2 Experimental Methods to Obtain Gob Material Size Distribution

In this paper, rock fragment size distribution data were taken from Pappas and Mark (1993). They conducted a laboratory study to estimate the gradation of actual gob material, to evaluate the stress–strain behavior of simulated gob material using load deformation tests. In this paper, the particle size gradation data were further analyzed with the developed models

Table 1 Summary of simulated materials (from Pappas and Mark 1993) analyzed in this paper and their loading tests

Test	Rock type	Maximum size (cm)	Maximum stress (MPa)	Initial porosity	Porosity @ 5.4 MPa	Porosity @ max. stress
A	Shale	5.1	19.0	0.802	0.365	0.160
B	Shale	8.9	21.3	0.679	0.269	0.078
C	Weak sst	5.1	19.3	0.790	0.313	0.152
D	Weak sst	8.9	21.1	0.719	0.337	0.162

"sst" in tests C and D stands for "sandstone"

to predict porosity and permeability. This section gives a brief description of the laboratory tests conducted by Pappas and Mark (1993).

2.1 Obtaining Rock Particle Gradation Curves for Tests

Pappas and Mark (1993) conducted laboratory tests on rock materials with properties similar to those of actual gob material. The characteristics considered were the tensile and compressive rock strengths, rock density, surface roughness, rock shape, rock size, and size gradation. Most of these characteristics would be simulated by broken rock obtained from fresh roof falls. They reduced the rock size and gradation to a laboratory scale by proportionally shifting the particle size distribution curve of the actual gob material determined from pictures taken from the headgate entries (Fig. 1) where portions of the gob could be viewed. This shift was performed parallel to the horizontal axis of the particle-size curve until the desired maximum particle size of the laboratory sample was reached. The detailed procedure for this can be found in Pappas and Mark (1993).

2.2 Load Deformation Tests on Fragmented Rocks

For load deformation tests on fragmented rock material, a test chamber was built in which the simulated gob material was subjected to different loads. The weight of the rock in the test chamber was determined by subtracting the weight of the chamber from the total weight. This value was used to calculate initial void volume, or porosity, of the simulated gob material. Then, the loading on the rock material was increased at a specified rate and load and displacement were monitored. The maximum load applied to the simulated gob material increased as the test series progressed.

Pappas and Mark (1993) conducted 20 tests by varying the maximum particle size in the simulated gob material and the maximum applied stress. In this paper, the size distributions obtained with maximum particle sizes of 5.1 cm (2 inches) for shale and weak sandstone were used for modeling and comparison purposes. These tests will be referred to as Test-A (shale-maximum size 5.1 cm), Test-B (shale-maximum size 8.9 cm), Test-C (weak sandstone-maximum size 5.1 cm), and Test-D (weak sandstone-maximum size 8.9 cm). Table 1 gives the test summary of each simulated gob material. Figures 2 and 3 show particle size distributions of shale and weak sandstone before and after loading tests. The data are for four tests conducted on two different initial size distributions with different initial maximum sizes.

Figure 4 shows the stress–strain data obtained during the loading tests. The data showed that the stress–strain behavior of simulated materials was non-linear, indicating a

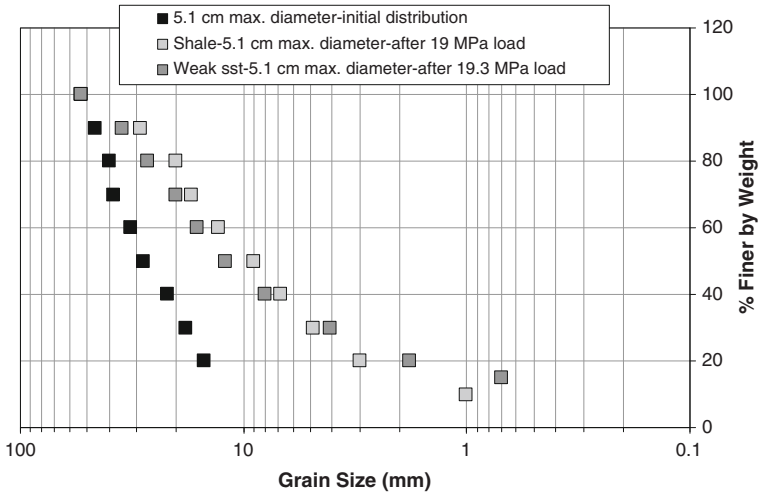

Fig. 2 Particle size distribution of shale before and after compressing the simulated gob material in the loading chamber

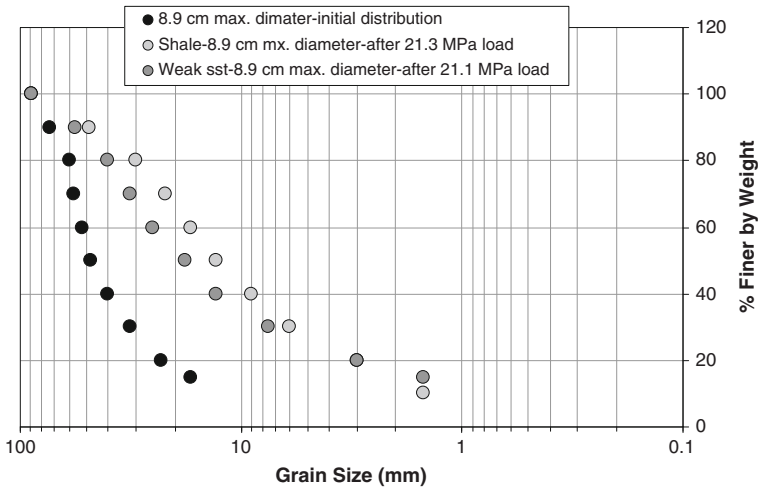

Fig. 3 Particle size distribution of weak sandstone before and after compressing the simulated gob material in the loading chamber

strain-hardening process during compression. Again, it was observed that the stress–strain behavior was not dramatically affected by the rock type. However, it was observed that as the maximum size of initial material increased from 5.1 cm to 8.9 cm, the granular medium experienced somewhat less compaction at higher stresses.

In the following sections, particle size distribution data of simulated gob material before and after loading tests (Figs. 2 and 3), as well as stress–strain data (Fig. 4), will be used to calculate various fractal dimensions of flow channels and rock skeleton. These techniques will develop a method for predicting porosity and permeability of a "fractal" gob during compaction from overburden stress.

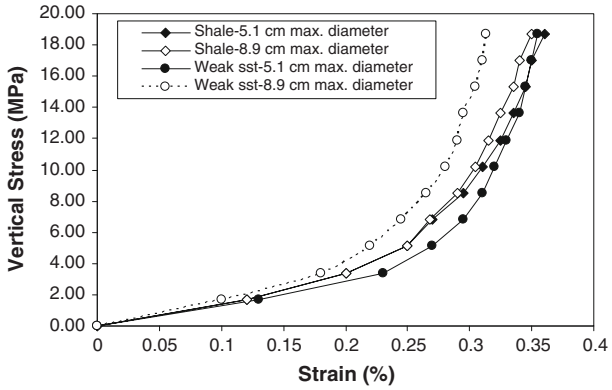

Fig. 4 Stress–strain curves for shale and weak sandstone of different initial particle distributions (Figs. 2 and 3) subjected to various vertical loadings in the test chamber

3 Theory and Model Development

3.1 Fractal Fragmentation

Fragmentation is a structural failure of a brittle material caused by multiple fractures of different lengths (Perfect 1997). The disordered nature of pores and grains in fragmented porous medium suggests that the structure created by the fragmentation process shows scaling properties (Weiss 2001). Fractal models not only can describe the scaling of mass and surface roughness of individual fragments but also the fragment size distributions.

Fragment size distribution and fragment density may influence the mechanics of fluids in the fragmented medium. However, an explicit formulation of the relationship between pore texture and the hydraulic properties of the porous media remains a challenge due to the complex pore-particle geometry. Yu and Liu (2004) presented fractal analyzes of permeabilities for both saturated and unsaturated porous media based on the fractal nature of pores. Schlueter et al. (1997) defined the pores of sedimentary rocks from thin sections and scanning electron microscope (SEM) images using a perimeter–area relationship. They discussed how the pore-area fractal dimensions and the grid sizes used to measure fractal dimensions can affect permeability predictions. Hydraulic properties in a fragmented porous medium can also be determined either from simple sieve analyzes or from a laser-diffraction analysis of the particles (Karacan and Halleck 2003). Bitelli et al. (1999) and Perfect and Kay (1995) used particle size data to calculate the fractal dimensions of different soil samples exposed to various operational and weathering conditions using the power law scaling of the number–particle size relation given by Turcotte (1986):

$$N(\omega > \Omega) = B_F \Omega^{-D_F}, \tag{1}$$

where N is the cumulative number of particles of size ω greater than a characteristic size Ω, the exponent D_F is referred to as the fragmentation fractal dimension and includes the information about the scale dependence of the number–size distribution of aggregates, and B_F is a coefficient related to number of particles of unit diameter.

The first attempt to directly relate the particle size distribution to a soil water characteristic was made by Arya and Paris (1981). In their model, pore lengths (based on spherical particles) were scaled to natural pore lengths using a scaling parameter α with an average

value of 1.38. This fitting parameter α was derived from least squares regression of the predicted water content to the measured water content and its use was justified by accounting for the non-spherical nature of the particles. Tyler and Wheatcraft (1989) interpreted α as the fractal dimension of a tortuous pore. Since, then, there has been growing interest in the use of fractals to predict hydraulic properties from particle size distributions (Rieu and Sposito 1991; Tyler and Wheatcraft 1992; Comegna et al. 1988).

3.2 Model Development for Predicting Permeability in a Fragmented Porous Medium Under Successive Compaction

3.2.1 Flow in Fractal Porous Media

In this study, the porous medium forming the gob was assumed to have pore sizes that can be considered as bundles of capillary tubes of different diameters as suggested by Yu and Cheng (2002). If the diameter of a capillary is assumed to be η and its tortuous length along the flow direction is $L_t(\eta)$, then the tortuous length will be longer than its representative length L_o, which runs the shortest distance between two points. For a straight capillary, the tortuous length equals the representative length. Following Wheatcraft and Tyler (1988) expression and scaling approach for flow in a heterogeneous medium, there is a fractal scaling between the diameter and length of the capillaries (Yu and Cheng 2002):

$$L_t(\eta) = \eta^{1-D_T} L_o^{D_T}. \tag{2}$$

In this equation, D_T is the tortuosity fractal dimension, which can take values between 1 and 2. D_T represents the convolutedness of flow channels. When D_T is 1, the flow channels are straight. The tortuosity increases with increasing values of D_T. In the limiting case of $D_T = 2$, we have a highly tortuous line that fills a plane (Wheatcraft and Tyler 1988). However, Wheatcraft and Tyler (1988) reported that D_T values more than 1.5 do not have any physical significance.

For the bundle of capillaries or flow channels, the number of channels with size η is also important. Since channels in a porous medium are analogous to the islands in a sea or spots on surfaces, the cumulative size distribution of pores can be written as:

$$N(L \geq \eta) = \left(\frac{\eta_{\max}}{\eta}\right)^{D_P}. \tag{3}$$

In this equation, N is the number of pores whose sizes (η) are greater than a characteristic size L and $\eta_{\max}$ is the maximum pore size. Equation 3 can be differentiated to give:

$$-\mathrm{d}N = D_P \eta_{\max}^{D_P} \eta^{-(D_P+1)} \mathrm{d}(\eta). \tag{4}$$

In Eq. 4, D_P is the pore-area fractal dimension ($1 < D_P < 2$). A D_P-value of 2 represents a regular pore area (circle, square etc.) and the irregularity increases for D_P <2. These equations describe the scaling relationship of cumulative pore populations. The total number of pores from the smallest diameter $\eta_{\min}$ to the largest diameter $\eta_{\max}$, thus, can be obtained from the Eqs. 3 and 4 as:

$$N_t(L \geq \eta_{\min}) = \left(\frac{\eta_{\max}}{\eta_{\min}}\right)^{D_P}. \tag{5}$$

Dividing Eq. 4 by Eq. 5 obtains an expression for the probability density function:

$$-\frac{\mathrm{d}N}{N_t} = D_P \eta_{\min}^{D_P} \eta^{-(D_P+1)} \mathrm{d}(\eta) = f(\eta)\mathrm{d}(\eta), \tag{6}$$

where

$$f(\eta) = D_P \eta_{\min}^{D_P} \eta^{-(D_P+1)}. \tag{7}$$

The equations above can be used as a model of a capillary tube bundle of any shape.

In order to characterize a pressure-driven, steady-state flow of a fluid through long, straight, and rigid channels of any constant cross-sectional shape, with no-slip boundary conditions, the Hagen–Poiseuille (H–P) flow equation can be used. For these flow conditions, the Navier-Stokes equation takes the form:

$$(\partial_x^2 + \partial_y^2) v(x, y) = \frac{\Delta P}{\mu L}. \tag{8}$$

H–P flow is often characterized by the hydraulic resistance, $\Pi_{\mathrm{hyd}} = \Delta P / Q$, in which ΔP is the pressure drop along the channel and Q is the flow rate. By including the drag and the effect of surface area, hydraulic resistance can alternatively be given as $\Pi^*_{\mathrm{hyd}} = \mu L / \mathrm{A}^2$. In this equation, μ is the dynamic viscosity of the fluid and L is the channel length. For an irregular shape on the x–y plane, the cross-sectional area "A" is defined as $\int_\Psi \mathrm{d}x\mathrm{d}y$. Using the same approach, $\int_{\Psi_p} \mathrm{d}l$ is the perimeter of the object. Then, the hydraulic radius can be defined as:

$$R_H = \frac{\int_\Psi \mathrm{d}x\mathrm{d}y}{\int_{\Psi_p} \mathrm{d}l} \tag{9}$$

Figure 5 shows an arbitrary cross section Ψ with perimeter Ψ_p in the x- and y-plane for a straight channel placed along the z-axis. In H–P flow, there is a no-slip boundary condition at the walls of Ψ_p, and thus the actual hydraulic resistance will depend on the perimeter as well as the cross-sectional area. This dependence can therefore be characterized by a dimensionless correction factor α for shape:

$$\alpha = \frac{\Pi_{\mathrm{hyd}}}{\Pi^*_{\mathrm{hyd}}}. \tag{10}$$

The relation between the pressure drop ΔP, the velocity $v(x, y)$, and the geometrical correction factor becomes:

$$\Delta P = \Pi_{\mathrm{hyd}} Q = \alpha \Pi^*_{\mathrm{hyd}} Q = \alpha \Pi^*_{\mathrm{hyd}} \int_\Psi \mathrm{d}x\mathrm{d}y v(x, y). \tag{11}$$

If this equation is solved for a circular area (circular pipe) of Ψ, we obtain:

$$Q_i = \frac{\pi \Delta P \eta^c}{16 \alpha \mu L_t}, \tag{12}$$

where η is the hydraulic diameter and L_t is the total length of the channel. In circular pipes, $\alpha = 8$ and the exponent "c" of the equivalent channel diameter is 4. For some known shapes,

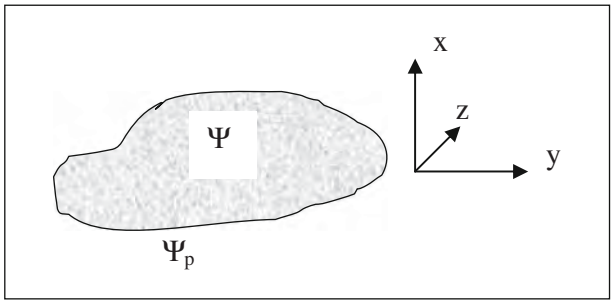

Fig. 5 An arbitrary cross section of a pore with cross sectional area Ψ and perimeter Ψ_p

such as ellipse, rectangle, and triangle, the shape correction factor (α) is given by Mortensen et al. (2005):

$$\text{For ellipse:}\alpha = 4\pi \quad \frac{a}{b} + \frac{b}{a} \quad , \tag{13}$$

where a is the half-length of the major axis and b is the half-length of the minor axis.

$$\text{For rectangular cross sections:}\alpha = \frac{\pi^3\gamma^2}{8}\left(\sum_{n=1,3,5\ldots}^{\infty}\frac{\gamma}{\pi n^4} - \frac{2}{\pi^5 n^5}\tanh\left(\frac{n\pi\gamma}{2}\right)\right)^{-1}, \tag{14}$$

where γ is the width-to-height (w/h) ratio of the rectangular channel (Mortensen et al. 2005). $\tanh(x)$ can be approximated to 1 if x is very large, which can be satisfied if γ is very large (slit shaped channels for example). In this case, Eq. 14 becomes:

$$\alpha = \frac{12\pi^5\gamma^2}{\pi^5\gamma - 186\zeta(5)}, \tag{15}$$

where $\xi(5)$ results from truncating the summation after fifth iteration in Eq. 14.

For a triangular cross section: $\alpha = 20\sqrt{3}$, if it is an equilateral triangle. If the cross section is another triangular shape, then:

$$\alpha = \frac{25}{17}C + \frac{40\sqrt{3}}{17}, \tag{16}$$

where $C = \frac{8(a+b+c)^2}{\sqrt{\frac{1}{2}(a^2+b^2+c^2)^2-(a^4+b^4+c^4)}}$. In this equation, a, b, and c are the side lengths of the triangular channel.

Arya et al. (1999) attempted to determine shape factor "α" and exponent "c" empirically using experimental flow data in different soils. As a result of their analysis performed on different soil textures and materials (clays, sands, and sandy loams), they found that the exponent of diameter "c", in Eq.12, varied between 2.808 and 4.714. The average of all tests indicated that this number is 3.531. For the shape correction factor α, however, they determined that the logarithm of α for different textures changed from 2.759 to 6.742, with an average of 5.507 (Arya et al. 1999). In this paper, the average diameter exponent, from Arya et al.'s study (3.531), will be used in the H–P equation (Eq. 12) to describe flow in single channels. The variable "α", will be retained in the equation to run parametric analyzes related to channel shape.

$$Q_i(\eta) = \frac{\pi}{16}\frac{\Delta P}{L_t(\eta)\alpha}\frac{\eta^{3.531}}{\mu} \tag{17}$$

If the total flow rate is calculated for each channel between the minimum and maximum sizes over the entire range of pore sizes, Eqs. 4 and 17 can be integrated to give the total flow rate:

$$\begin{aligned} Q_T &= -\int_{\eta_{\min}}^{\eta_{\max}} Q_i(\eta)\mathrm{d}N(\eta) \\ &= \frac{\pi}{16}\frac{\Delta P}{\mu}\frac{L_o^{-D_T}}{\alpha}\frac{D_P}{2.531 + D_T - D_P}\eta_{\max}^{2.531-D_T}\left[1 - \left(\frac{\eta_{\min}}{\eta_{\max}}\right)^{2.531+D_T-D_P}\right]. \end{aligned} \tag{18}$$

Equation 18 honor the properties of H–P equation, where the streamlines are formed by individual particle sizes that create tortuous pores of a particular dimension and shape and those they do not really mix. Combining Eq. 18 with Darcy's Law:

$$Q_T = \frac{kA_T\Delta P}{\mu L_o}, \tag{19}$$

where k is the permeability and A_T is the total area to flow, yields the definition of permeability for a porous medium composed of tortuous channels of varying diameters and shapes:

$$k = \frac{\pi}{16A_T}\frac{L_o^{1-D_T}}{\alpha}\frac{D_P}{2.531 + D_T - D_P}\eta_{\max}^{2.531+D_T}\left[1 - \left(\frac{\eta_{\min}}{\eta_{\max}}\right)^{2.531+D_T-D_p}\right]. \tag{20}$$

Although Eq. 20 is a description of permeability in a general porous medium, the structural parameters embedded in A_T, for example, need to be defined.

3.2.2 Establishing Total Area "A_T" for Flow and Porosity for Completely Fragmented Porous Media

Total area of flow is the combination of areas for both pores and the rock surface exposed to the flow. This area gives the superficial velocity in the porous medium. If only the areas of pores are taken account, this will be the interstitial velocity, which is the average velocity in the actual pores or channels of the medium. Since, the gob material in the caved zone is highly fragmented and the total channel area is the same as the effective porosity where the flow occurs, total channel area (A_P) is used for A_T. In order to determine the value of A_P, the areas of individual flow channels can be summed mathematically as (Rieu and Sposito 1991):

$$A_T = A_P = \sum_{i=1}^{N} A_{P_i}. \tag{21}$$

In Eq. 21, A_{P_i} is the pore area fractions.

Tyler and Wheatcraft (1989) conceptualized the flow channels as tubes in a close-packed arrangement of grains and expressed the pore-size/grain-size relation with the following equation by replacing the scaling term α, in the Arya and Paris model (1981), by the tortuosity fractal dimension:

$$\eta_i = \Omega_i\left(\frac{2}{3}\phi_i N_i^{1-D_T}\right)^{1/2}. \tag{22}$$

In this equation, N_i is the number of particles of a certain size (Ω_i) lining up to create the tortuous channel with diameter η_i and tortuosity fractal dimension D_T. In Eq. 22, ϕ_i is the partial porosity in each particle size class. The summation of partial porosities gives the total (or effective) porosity of the fragmented porous medium ϕ_T (Rieu and Sposito 1991).

When Eq. 22 is inserted into Eq. 21, the total area is obtained in terms of particle size and partial porosities:

$$A_T = A_p = \sum_{i=1}^{s} \left(\frac{\pi \Omega_i^2}{6} \phi_i N_i^{1-D_T} \right). \tag{23}$$

Rieu and Sposito (1991) defined the virtual pore-size fraction concept for porosity. If a fractal porous medium, whose porosity results from a broad range of pore sizes, decreasing in mean diameter from η_o to η_{s-1}(s $\geq$ 1), is divided into "*s*" virtual pore-size fractions, then the total porosity is the summation of all partial porosities. Since the pores are assumed to be formed in a packing arrangement of the grains and the relation of η_i (mean pore diameter in the *i*th virtual pore-size fraction) with Ω_i is given by Eq. 22, then the number of pore-size classes can assumed to be equal to the number of particle size classes.

By using the virtual pore-size fraction concept and introducing the pore coefficient Γ, the ratio of successive increments of pore volume to the corresponding partial volumes, partial porosity can be written as (Rieu and Sposito 1991):

$$\phi_i = 1 - (1 - \Gamma)^{s-i} \tag{24}$$

Pore coefficient Γ is closely related to the fractal dimension D_F as:

$$\Gamma = 1 - r^{3-D_F} \quad (\Gamma < 1, r < 1), \tag{25}$$

where "*r*" is a similarity ratio that scales the pore sizes in a fractal porous medium. Using these relations, the porosity of a completely fragmented porous medium is given as:

$$\phi = 1 - (r^{3-D_F})^s. \tag{26}$$

This equation, in terms of particle sizes, gives total porosity as:

$$\phi_T = 1 - \left(\frac{\Omega_{\min}}{\Omega_{\max}} \right)^{3-D_F}, \tag{27}$$

where D_{F} is the fragmentation fractal dimension that can be determined from the slope of the *best linear fit* to the number–size relation given in Eq. 1.

3.2.3 Plastic Reduction in Porosity with Applied Stress Increment in Uniaxial Compression

In the caved zone of longwall gobs, the degree of compaction is a function of initial porosity and strength of the rock fragments. The initial porosity varies with the shape of rock fragments, their sizes, and size distribution (Yavuz 2004). As compression increases, the broken material will stiffen due to the densely compacted material and a reduction in porosity in the caved zone will result by further crushing or fragmentation of the initial rock pieces. Crushing is accompanied by changes in particle size distribution, which can be measured by various methods, such as sieving or laser-light scattering (McDowell et al. 1996).

Using the principles of grain crushing and a particle size distribution modeled as a self-similar pattern, the plastic reduction in porosity with a one-dimensional applied stress increment is given by (McDowell et al. 1996):

$$\mathrm{d}\phi_T = -\beta f^{\frac{(1-D_F)}{2}} \frac{\varepsilon}{(1-\kappa)\bar{\sigma}\,\Omega_{\max}} (2-D_F) m \sigma_0^{\frac{m(1-D_F)}{2}} \bar{\sigma}^{\frac{m(D_F-1)}{2}-1} \mathrm{d}\bar{\sigma} \tag{28}$$

In this equation, D_F is the fragmentation fractal dimension defined by Eq. 1, ε is the surface energy in linear-elastic fracture mechanics (Griffith 1920), m is the Weibull modulus based on the observations that particle-survival probability follows a Weibull distribution, σ_0 is the tensile strength of the grains, $\bar{\sigma}$ is the applied macroscopic stress, and f is fracturing probability term (McDowell et al. 1996). This equation can be written in a more compact form by separating it into the plastic compressibility index (Λ) and stress increment ($\mathrm{d}\bar{\sigma}$) terms:

$$\mathrm{d}\phi_T = -\Lambda \bar{\sigma}^{\frac{m(D_F-1)}{2}-2} \mathrm{d}\bar{\sigma}, \tag{29}$$

where Λ is defined as:

$$\Lambda = \beta f^{\frac{(1-D_F)}{2}} \frac{\varepsilon}{(1-\kappa)\bar{\sigma}\,\Omega_{\max}} (2-D_F) m \sigma_0^{\frac{m(1-D_F)}{2}}. \tag{30}$$

Equation 29 can be integrated, assuming Λ is constant at each stress level, between two successive stress increments (i to $i+1$) to obtain:

$$\phi_{T_{i+1}} - \phi_{T_i} = -\Lambda \left[\frac{\bar{\sigma}_{i+1}^{\frac{m(D_F-1)}{2}-1}}{\frac{m(D_F-1)}{2}-1} - \frac{\bar{\sigma}_i^{\frac{m(D_F-1)}{2}-1}}{\frac{m(D_F-1)}{2}-1} \right]. \tag{31}$$

In order to solve Eqs. 28–31, the plastic compressibility index (Λ) should be defined by using either substituting typical values of physical parameters in Eq. 30 or a typical value of 0.1 for sands and clays (McDowell et al. 1996).

4 Results and Discussion

4.1 Description of Fractal Model Parameters and their Calculations

In order to predict gob porosity and permeability under increasing compressive stresses, Eqs. 20, 23 and 27 (Eqs. 28–31 for porosity change under compression) should be evaluated. In effect, Eqs. 28–31 evaluate the change in porosity as a function of increasing vertical stress and fragmentation fractal dimension. The new porosity replaces the porosity term (ϕ_i) in Eq. 23 to modify the flow area (A_T). Finally, the updated flow area is inserted into Eq. 20 to estimate the permeability at a particular stress and fragmentation level.

The general solution procedure stated above requires determination of these parameters:

- Representative length (L_o)
- Maximum and minimum particle dimensions, Ω_{min} and Ω_{max}, in the range(s) that shows fractal behavior.
- Weibull modulus (m)
- Pore, tortuosity, and fragmentation fractal dimensions, D_P, D_T, and D_F, respectively.
- Virtual pore-size classes (s)
- Pore coefficient (Γ) and similarity ratio (r).
- Minimum and maximum pore (channel) diameters, η_{min} and η_{max}.

Weibull modulus (m) is a measure of the variability in strength of the material. It increases with decreasing the variability in strength in the particle. For chalk, brick, stone, and cement,

m is between 1 and 5 (McDowell et al. 1996). Similar values would be expected for carbonates. As "m" decreases, the impurities or structural variabilities in the grains increase and the strength of the material decreases. Thus, a low m-value around 2 should be expected for natural materials.

Most flow occurs in the horizontal directions within the gob due to the pressure differentials between points in the gob and the nearest gateroad or longwall face. Representative length (L_o) thus is defined as the shortest distance between two points, where there is a pressure differential that drives the flow. These two points may be on either side of the measurement interval within the gob or from a point in the gob to the gateroads. According to Eq. 2, when there is no convoluteness ($D_T = 1$), the length of a straight channel is equal to the representative length in any flow direction. Therefore, the representative lengths change based on the location of the evaluation points in the gob. In this paper, L_o was taken as 10 m. The porosity and permeability values are representative of 10 m long segments in the flow direction, experiencing an average macroscopic stress of $\bar{\sigma}$.

Fragmentation fractal dimension (D_F) must be <3 (Kozak et al. 1996) in order for the probability of grain fragmentation to be <1 (Comegna et al. 1988). A fractal dimension between 0 and 3 reflects a population dominated by relatively larger particles and by a distribution dominated by smaller particles (Turcotte 1986) as the value approaches 3. It has also been reported that confinement under compression impacts fractal dimension with lower fractal dimensions caused by relatively unconfined conditions and higher fractal dimensions approaching 3 resulting from extensive grinding caused by high confinement.

In the study of Pappas and Mark (1993), the particle-size data was reported as a distribution of mass percent of total particles passing through a certain sieve size (Figs. 2 and 3), rather than the actual number of particles. Therefore, initial mass was calculated using volume of the test chamber and assuming a constant rock density of 2.3 g/cc for shale and 2.5 g/cc for sandstone. From this data, the number of particles in each size class (sieve size) was calculated by assuming that the particles are spherical in shape. Example linear fits to the number–size data are given in Fig. 6 (for tests A and B, before loading and after loading). These data show that fragmentation fractal dimensions have increased after the loading tests indicating the presence of a finer particle size produced during crushing.

The cumulative number versus particle size relation (Fig. 6), which is used to determine D_F can also be used to find the maximum and minimum particle size (Hunt and Gee 2001). Maximum and minimum particle diameters (Ω_{min} and Ω_{max}) are approximately the limits of the linearity in the number–size relation. However, it should be noted that there is a deviation from linearity in Fig. 6 (minimally in A and more in B before loading). This may be related due to multi-fractal distribution of rock particle size classes before loading. In this case, a piecewise analysis of the data is a possibility. However, toward larger particle diameters where a large portion of porosity may reside, the slope becomes >3, which physically is not possible. Thus, in order not to exclude that porosity in the initial material, it was assumed that linearity in the log–log behavior in Fig. 6 is maintained for all cases through the entire range of particle sizes.

The fragmentation fractal dimensions and maximum and minimum particle sizes before and after loading tests are listed in Table 2. This table shows that after loading, fragmentation fractal dimensions of the initial particle size distributions have increased indicating the shift in maximum and minimum particles sizes created during crushing, as shown in Figs. 2 and 3.

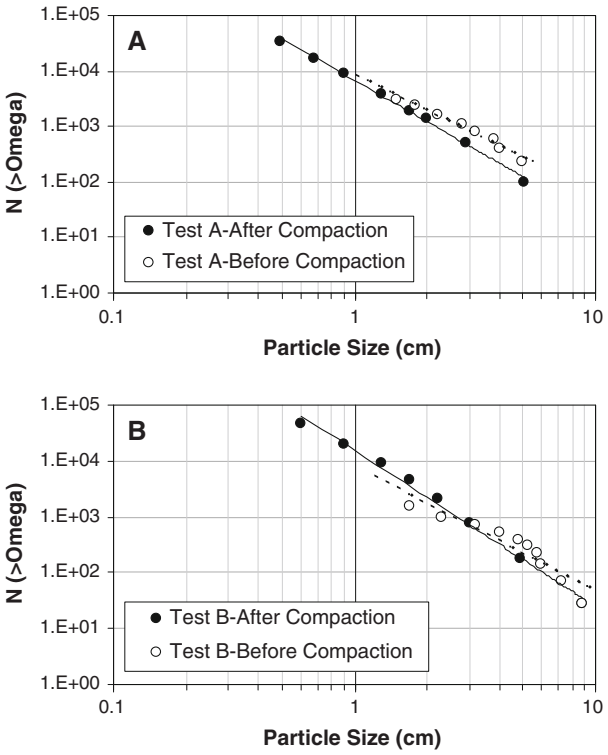

Fig. 6 Log–log plots for number–particle size data (Eq. 1) for Tests A and B *before* and *after* loading. D_F's for Test A—before compaction and after compaction are 2.19 and 2.89, respectively. D_F's for Test B—before compaction and after compaction is 2.25 and 2.91, respectively

Table 2 Results of D_F and maximum (Ω_{max}) and minimum (Ω_{min}) particle sizes determined before and after loading tests using number–size relationship

Test	Before loading				After loading			
	s	D_F	Ω_{min}(cm)	Ω_{max} (cm)	s	D_F	Ω_{min} (cm)	Ω_{max} (cm)
A	9	2.19	1.5	5.1	10	2.89	0.5	5.1
B	10	2.25	1.7	8.9	10	2.91	0.6	8.9
C	9	2.19	1.5	5.1	10	2.81	0.4	5.1
D	10	2.25	1.7	8.9	10	2.87	0.8	8.9

The number of virtual pore-size classes "*s*" is equal to the number of different particle size fractions that are within the data set where fractal scaling is observed. Since a linear trend is accepted between all particle size classes (Fig. 6), the number of particle size classes used will be the same as the virtual pore-size fractions (Table 2). The pore coefficient Γ, which is the ratio of successive increments of pore volume to the corresponding partial volumes and the similarity ratio r that scales the pore sizes in a fractal porous medium can be calculated using Eqs. 25 and 26.

Fractal dimension of the one-dimensional trace of pore channel (D_T), or tortuosity fractal dimension, describes how the pores are convoluted in relation to L_o. However, it is not always easy to determine the tortuosity of a channel to find its fractal dimension. In this study, the "slit-island" theorem of Mandelbrot et al. (1994) was used to determine D_T, since there is

really no practical means of measuring this parameter. Mandelbrot et al. (1994) proposed that "the difference between an object's fractal dimension and its topological (or Euclidean) dimension could be described as the fractal increment or FI." They further suggested that this fractal increment could be used to estimate the fractal dimension of lower-order topological units. For example, a line drawn on a fractal surface will have the same FI as the surface. If the fractal dimension of the surface is 2.5 and its FI is 0.5 ($2.5 - 2.0 = 0.5$), then the fractal dimension of a line drawn across this surface will be 1.5 ($1.0 + 0.5 = 1.5$). This approach has been used in the literature (Sammis and Steacy 1995) to estimate the fractal dimension of lower-order geometries.

In order to apply the slit-island theorem to estimate the tortuosity fractal dimension (D_T) in the crushed material, the fractal increment values reported by various researchers on different type of soil and porous rocks were evaluated. Jacquin and Adler (1988) observed fractal increments of 0.23 in pore structures of dolomitic limestone. Tyler and Wheatcraft (1989) reported fractal increments between 0.14 and 0.43, with an average of 0.23, when obtained from soil particle size data. Karacan and Halleck (2003) determined that an average D_T increment of 0.29 for incompletely fragmented porous media by shock waves. These increments can be used to calculate D_T values of 1.23 and 1.29 from these references for highly compacted and incompletely fragmented porous media, respectively. The average of these two values (1.26) will be taken as the representative value for the compacted gob. For the initial gob material, 1.10 will be used as the average of D_T. This value is based on the averages calculated by Wheatcraft and Tyler (1988) as 1.08 using Monte-Carlo simulations, values reported by Yu and Cheng (2002), and Yu and Liu (2004) for pores in 52% porosity medium between 1.10 and 1.12. These values have physical sense, since compaction or incomplete fragmentation compared to complete fragmentation increases the tortuosity of pore channels.

If the pore area represents a smooth object (circle, square, triangle etc.) covering the whole area, then D_P can be taken as 2. If the pores are irregular in shape and distribution, then their area-fractal dimension will be less than 2 (Ahmed and Drzymala 2005). In case of irregular pore shapes and distributions, slit-island theorem can be used by employing the D_F values (Table 2) obtained in this study. Since particle size distribution is a 3-dimensional entity (Tyler and Wheatcraft 1989), its Euclidean dimension is 3. Then, the calculated increments ($D_F - 3$) are added to the Euclidean dimension for area to obtain D_P. The calculated values are less than 2 (Table 3).

Tortuosity (D_T) and pore-area (D_P) fractal dimensions for straight and regular pores as well as the values determined using the above approaches for the convoluted and irregular pores are given in Table 3. These values will be used in model calculations later in this paper.

4.2 Up-Scaling Particle Sizes used in Experiments to Actual Gob Material

Pappas and Mark (1993) simulated the gob material to determine the tensile and compressive rock strengths, rock density, surface roughness, and rock shape. However, they scaled down the grain-size distribution curves for determining the stress–strain properties of granular materials representing a gob. The ratio of scaling between actual and laboratory gob material was approximately 10.

In order to calculate porosity and permeability using actual gob-material sizes and their distributions, the gradation curves (Figs. 2 and 3) were up-scaled by 10 times to their original sizes. Up-scaling, in effect, changes particle sizes and eventually the channel sizes that will be calculated based on particle size. However, as long as the gradation curve is held constant, up-scaling does not change the fragmentation fractal dimensions since this will not

Table 3 D_T and D_P values determined for the tortuous and irregular flow channels and straight and smooth channels

Test	$D_{T\,(\text{straight})}$	$D_{T\,(\text{tortuous})}$	$D_{P\,(\text{uniform})}$	$D_{P\,(\text{irregular})}$
Before loading				
A	1	1.10	2	1.19
B	1	1.10	2	1.25
C	1	1.10	2	1.19
D	1	1.10	2	1.25
After loading				
A	1	1.26	2	1.89
B	1	1.26	2	1.91
C	1	1.26	2	1.81
D	1	1.26	2	1.87

Table 4 Up-scaled particle sizes for different tests before and after loading

Before loading			After loading		
Test	$\Omega_{\min}$ (cm)	$\Omega_{\max}$ (cm)	Test	$\Omega_{\min}$ (cm)	$\Omega_{\max}$ (cm)
A	15	51	A	5.0	51
B	17	89	B	6.0	89
C	15	51	C	4.0	51
D	17	89	D	8.0	89

change the slope. Thus, the fractal dimensions reported in Tables 2 and 3 will still be valid. Table 4 shows the up-scaled maximum and minimum particle sizes under the assumption of scale-invariant fragmentation.

4.3 Porosity of Initial and Compacted Gob Material

4.3.1 Calculation of Porosity Reduction from Stress–Strain Behavior and from Fractal Model (Eq. 27) Before and After Compaction

Before calculating the porosities using particle size distributions and the theory described in Sect. 3, porosities that should be experienced in the gob were calculated using the experimental stress–strain curve (Fig. 4) and the initial porosities given in Table 1. The results of this calculation are shown in Fig. 7.

The porosity evaluation during uniaxial compression of simulated gob material shows that at earlier loadings, the material could be compressed more when compared to later stages as also suggested by their stress–strain behavior. At around a stress level of 19 MPa (2,750 psi), the final porosities were roughly 10% for Test B, and 19–20% for the other tests. These numbers are close to the final porosities given in Table 1. It should be noted that the final values reported in Table 1 were obtained at higher stress levels. Thus, a difference of 3–4% between the values given in Fig. 7 and the values in Table 1 can be considered close for this analysis. As an inner check point, the porosity values reported for 5.4 MPa (800 psi) were compared with the corresponding data shown in Fig. 8. These values are also within 1–2% of

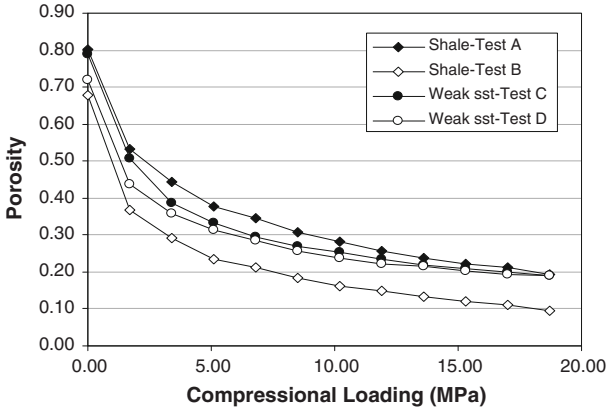

Fig. 7 Porosities calculated for compacting gob materials under compressive loading

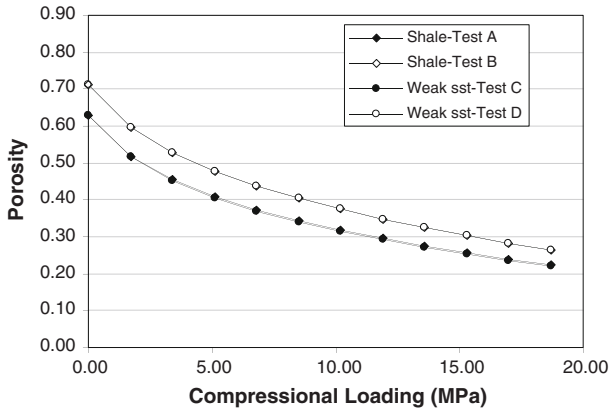

Fig. 8 Porosities predicted for compacting gob materials using Eqs. 28– 31

each other. Thus, the data of Fig. 7 will be used to compare with the porosity values calculated using fractal models (Eq. 24–31).

Initial and final porosities before and after compaction can also be calculated using fractal model (Eq. 27) and the particle size distributions of fragmented material. The porosity values obtained using Eq. 27 and the values determined in the laboratory before loading are compared in Table 5. The pore coefficients Γ and similarity values r calculated using Eq. 25 and 26, respectively, for the initial gob material are also given in Table 5. The porosity predictions given in this table are usually within 15% compared to laboratory measurements. This difference can be attributed to the nature of independent measurements and calculations.

Table 5 also shows the pore coefficients Γ and similarity values r calculated by using predicted porosity values in Eqs. 25 and 26. The values of these two numbers should be <1. The pore coefficient Γ in a fractal porous medium can be interpreted as the partial porosity contributed to each partial volume by pores of a certain size. Similarity number r, on the other hand, is a linear similarity ratio that relates successive pore sizes by their particle sizes (Rieu and Sposito 1991). Thus, having close and high r-values indicate close scaling relations between each pore and size class.

Table 5 Comparison of porosities determined in the laboratory with the predictions using Eq. 27 for before-loading cases

Test	Porosity-$\emptyset_L$-(laboratory)	Porosity-$\emptyset_P$-(Predicted) (Eq. 27)	$r_{\emptyset_p}$ (Eq. 26)	$\Gamma_{\emptyset_p}$ (Eq. 25)
A	0.802	0.629	0.873	0.104
B	0.679	0.711	0.847	0.117
C	0.790	0.629	0.873	0.104
D	0.719	0.711	0.847	0.117

The pore coefficients, Γ, and similarity ratios, r, for a fractal porous medium for both sets of porosity values are also given

Table 6 The porosities, pore coefficients, Γ, and similarity ratios, r, for a fractal porous medium, calculated using the crushed material size distribution data obtained after loading

Test	Porosity @ max. stress (Table 1)	Final porosity from strain (Fig. 7)	Porosity -$\emptyset_P$- (Predicted) (Eq. 27)	$r_{\emptyset p}$ (Eq. 26)	$\Gamma_{\emptyset p}$ (Eq. 25)
A	0.160	0.19	0.225	0.793	0.025
B	0.078	0.09	0.216	0.764	0.024
C	0.152	0.19	0.383	0.775	0.047
D	0.162	0.19	0.269	0.786	0.031

The porosities of simulated gob material after loading tests were also calculated by using the particle size distributions data after the tests and the fractal model given in Eq. 27. For these calculations, lower bounds of the particle diameters after loading, where linear number–size relations were observed, were determined as 0.5, 0.6, 0.4, and 0.8 cm (5, 6, 4, and 8 cm for up-scaled diameters) for tests A, B, C, and D, respectively. The porosity values obtained using fractal fragmentation data in Eq. 27 and the porosities determined in the laboratory after loading tests and using the strain data are compared in Table 6. The pore coefficients Γ and similarity r-values calculated using Eq. 25 and 26, respectively, are also given in Table 6. This table shows that predicted porosities after loading are lower than the calculated initial porosities (Table 5) due to crushing of grains. The comparison of predicted porosities in Table 6 with the values calculated using strain data (Fig. 7) and with the reported porosities at maximum stress show that the values calculated using non-fractal methods are somewhat lower compared to the predicted ones.

4.3.2 Predicting Compaction "Path" of Gob Material and Evolving Porosities Using Fractal Crushing Model

Progressively increasing stresses during mining compacts the initial gob material until it can fully support the weight of the overburden. This stress reestablishment happens at a certain distance from the longwall face. During the stress reestablishment period, the reservoir properties of the gob material continue changing as a result of compaction and crushing under increasing stress. In this section, the application and the results of the fractal crushing method introduced in Sect. 3 are discussed for its potential to model gob compaction.

Porosities were calculated using fractal compression and crushing models presented in Eqs. 28–31. The results of these calculations are shown in Fig. 8. In the calculations using these equations, the plastic compressibility index Λ was taken as 0.1 as suggested by McDowell et

al. (1996). The Weibull modulus m, on the other hand, was taken as 2.0, considering the fact that shale and weak sandstone are natural materials with many defects to lead to their high probability of fragmentation. The initial porosities plotted in Fig. 8 are the predicted initial porosities given in Table 5.

Figure 8 shows that as stress increases, the predicted porosities using the fractal model (Eqs. 28–31) decrease in a manner similar to Fig. 7. Also, considering the use of predicted initial porosities given in Table 5 and the use of Weibull and plastic compression constants together with the fragmentation fractal dimensions given in Table 2 for the initial number–size distribution of simulated gob material, the predicted porosity values are very close to calculations shown in Fig. 7, as well as to the final porosities given in Table 6. This suggests that one can use the initial number–size distribution of a granular media and its fragmentation fractal dimension to calculate changing porosities as stress is progressively increased. In Fig. 8, the initial porosities and fragmentation fractal dimensions are the same for each of the two test pairs (A–C) and (B–D) and their predicted porosities coincide as opposed to being separate as in Fig. 7.

4.4 Calculation of Permeability of Gob Material

4.4.1 Determining Flow Area of Channels (A_P) in the Fractal Porous Medium

In order to calculate gob permeability, Eq. 20 was used. The permeability equation requires flow area of pores (A_P, Eq. 23) and maximum and minimum channel sizes to be known. The size of the grains in a fragmented porous media will directly affect the pore flow area and pore diameters forming between the grains. Also, as compression increases on the initial gob material, the porosity will decrease as discussed in the previous section. In order to calculate permeability under increasing loading, up-scaled grain sizes will be used in area- and pore-size calculations. In order to incorporate the effect of loading on permeability, a fractal crushing model for porosity will be integrated into calculations.

Equation 23 is used to calculate the total flow area of pores. This equation can alternatively be represented with an integral:

$$\frac{\pi}{3}\int_{\Omega_{\min}}^{\Omega_{\max}} \Omega\phi N^{1-D_T}\,\mathrm{d}\Omega. \tag{32}$$

In this integral, maximum and minimum particle sizes are the up-scaled values and the number (N) is a function of grain size (Ω). In order to find this function, the numbers of up-scaled particles for each up-scaled size were plotted. By up-scaling the material mass (assuming density stays constant) by 1,000 times due to a 10-fold increase in particle diameter, the number–size relations are obtained. The functional relationships for these number–size plots are given in Table 7. These equations show that the number–size data can be successfully represented by power functions. The R^2 values of the equations representing the data in Table 7 are about 0.9927.

In Eq. 32, Ø-values are the partial porosities for each infinitesimal size interval. Integration between $\Omega_{\min}$ and $\Omega_{\max}$ will result in the total fractal porosity ($Ø_T$), which will not be dependent on Ω. With these treatments, the fractal flow area (Eq. 32), for Test-A for example,

Table 7 Functional relationships of number of particles as a function of up-scaled particle diameters (Ω is in cm)

Test	N
A	$10326.0\ \Omega^{-1.74}$
B	$8176.7\ \Omega^{-1.75}$
C	$9687.1\ \Omega^{-1.74}$
D	$7158.0\ \Omega^{-1.75}$

Table 8 Flow areas calculated for the initial gob material for Tests A-D. Particle diameters are the up-scaled values and their units are in cm

Test	A_P (Eq. 23)
A	$\frac{10326^{1-D_T}\pi}{3}\phi_T\left[\frac{\Omega_{max}^{0.26+1.74D_T}}{1.74D_T+0.26}-\frac{\Omega_{min}^{0.26+1.74D_T}}{1.74D_T+0.26}\right]$
B	$\frac{8176.7^{1-D_T}\pi}{3}\phi_T\left[\frac{\Omega_{max}^{0.25+1.75D_T}}{1.75D_T+0.25}-\frac{\Omega_{min}^{0.25+1.75D_T}}{1.75D_T+0.25}\right]$
C	$\frac{9687.1^{1-D_T}\pi}{3}\phi_T\left[\frac{\Omega_{max}^{0.26+1.74D_T}}{1.74D_T+0.26}-\frac{\Omega_{min}^{0.26+1.74D_T}}{1.74D_T+0.26}\right]$
D	$\frac{7158^{1-D_T}\pi}{3}\phi_T\left[\frac{\Omega_{max}^{0.25+1.75D_T}}{1.75D_T+0.25}-\frac{\Omega_{min}^{0.25+1.75D_T}}{1.75D_T+0.25}\right]$

becomes:

$$\frac{\pi}{3}\phi_T\int_{\Omega_{min}}^{\Omega_{max}}(10326\Omega^{-1.74})^{1-D_T}\Omega d\Omega. \tag{33}$$

Solving the integral gives the fractal pore area. The fractal flow areas calculated for the initial gob material of all tests are given in Table 8. These equations can be directly used in permeability equation (Eq. 20) for flow area term. In these equations, $\emptyset_T$ is the porosity which changes as uniaxial stress progressively increases according to Eqs. 28–31.

4.4.2 Determining Size of Tortuous Flow Channels (η)

In order to determine maximum and minimum channel sizes, Eq. 22 is used. This equation gives the sizes of flow channels in each partial volume of a fractal porous medium. In this equation, the number term (N) is replaced by its functional form given in Table 7. The partial porosity term in the equation is, on the other hand, the amount of porosity in that partial volume. In order to obtain partial porosity, the total porosity at a particular loading stage can be divided by the "virtual pore-size fractions" or the number of particle size classes "s" defined earlier in this paper (Table 2). With these additions, the maximum and minimum channel diameters (η_{max} and η_{min}) as a function of Ω can be calculated. These relations are given in Table 9.

Table 9 Minimum and maximum sizes ($\eta_{\min}$ and $\eta_{\max}$) of tortuous flow channels as a function of particle size

Test	$\eta_{\max}$ (Eq. 22)	$\eta_{\min}$ (Eq. 22)
A	$0.82\sqrt{\frac{\phi_T}{s}(10236^{1-D_T})\Omega_{\max}^{0.26+1.74D_T}}$	$0.82\sqrt{\frac{\phi_T}{s}(10236^{1-D_T})\Omega_{\min}^{0.26+1.74D_T}}$
B	$0.82\sqrt{\frac{\phi_T}{s}(8176.7^{1-D_T})\Omega_{\max}^{0.25+1.75D_T}}$	$0.82\sqrt{\frac{\phi_T}{s}(8176.7^{1-D_T})\Omega_{\min}^{0.25+1.75D_T}}$
C	$0.82\sqrt{\frac{\phi_T}{s}(9687.1^{1-D_T})\Omega_{\max}^{0.26+1.74D_T}}$	$0.82\sqrt{\frac{\phi_T}{s}(9687.1^{1-D_T})\Omega_{\min}^{0.25+1.74D_T}}$
D	$0.82\sqrt{\frac{\phi_T}{s}(7158^{1-D_T})\Omega_{\max}^{0.25+1.75D_T}}$	$0.82\sqrt{\frac{\phi_T}{s}(7158^{1-D_T})\Omega_{\min}^{0.25+1.75D_T}}$

Particle diameters to be used are the up-scaled values. The units of both particle sizes and the resulting channel sizes are in cm

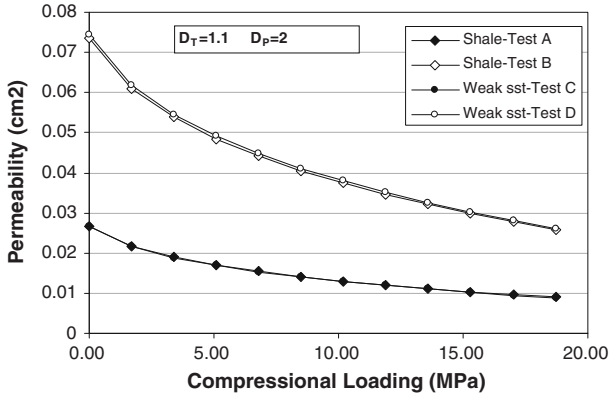

Fig. 9 Predicted permeabilities for gob simulated in Tests A–D assuming circular channels with $D_T = 1.1$

4.4.3 Predicting Permeabilities for Circular Flow Channels with Different Tortuous Paths and for Pore Area Irregularities

Figure 9 shows the predicted permeability of gob material composed of broken rocks and circular flow channels as a function of uniaxial compressive load for shale and weak sandstone. Figure 9 shows that the permeability is higher initially and decreases as a result of crushing and compaction during loading. The predicted permeabilities are changing from $0.074\,\text{cm}^2$ (74×10^5 Darcy) to $0.026\,\text{cm}^2$ (26×10^5 Darcy) for a gob initially composed of bigger rocks and from $0.026\,\text{cm}^2$ (26×10^5 Darcy) to $0.009\,\text{cm}^2$ (9×10^5 Darcy) for smaller rock particles. The data shows that the percent reduction in permeability is close in both cases, around 65%. Figure 9 also shows that permeabilities are mainly affected by the size of the initial material, rather than the type of rock. This is partly due to using the same Weibull moduli (m) and plastic compressibility index (Λ) in the porosity reduction equations. Nevertheless, this observation is consistent with the expectations since bigger particles are prone to leave more pore space when they are casually dumped into a finite volume.

The predicted permeabilities in Fig. 9 with $D_T = 1.1$ and $D_P = 2$ conditions may be considered as an optimistic approach for permeability calculation, since circular pores with no irregularities and relatively low tortuosity may result in higher permeability than it actually is for a gob environment. Thus, the complexity of the model environment was increased

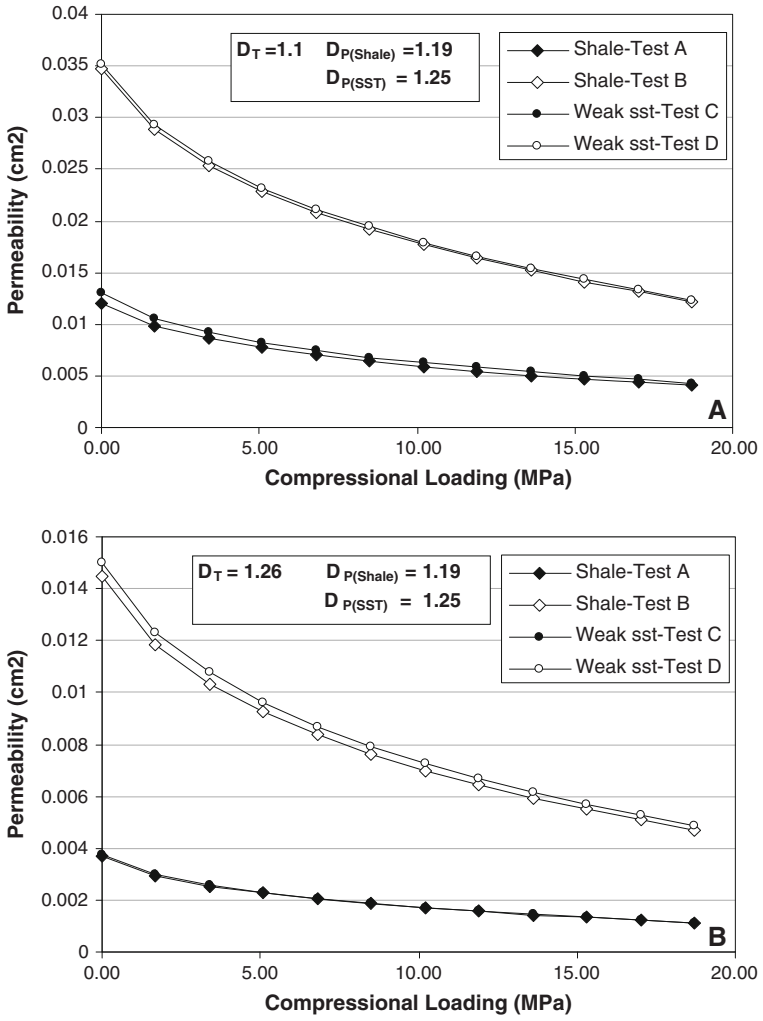

Fig. 10 Predicted gob permeabilities for different D_{P}-values of 1.19 for shale and 1.25 for sandstone (**a**), and with additional increasing flow channel tortuosity ($D_{\mathrm{T}} = 1.26$) (**b**)

by changing the D_T- and D_P-values. D_P-values were changed to 1.19 for shale and 1.25 for weak sandstone as presented in Table 3 for the initial gob material. D_T, on the other hand, was increased to 1.26 based on literature data discussed in Sect. 4.1. It is also interesting to note that a D_T of 1.26 is almost the mid-point between 1 (straight channel) and 1.5 after which tortuosity fractal dimension does not have a physical meaning according to Wheatcraft and Tyler (1988). The gob permeabilities predicted for more tortuous and irregular circular channels using the updated D_T- and D_{P}-values are shown in Fig. 10a, b.

Figure 10a, b shows that as the complexity of the flow path and the irregularity of pore areas increase, the permeability of the fragmented porous medium decreases. This is in agreement with the physical situation and with the practical experiences. For instance, for the case presented in Fig. 10a, when the irregularity of circular channels is increased, the permeability values decrease by almost 50% compared to the values shown in Fig. 9 that

represent perfectly circular channels. In addition to this, when we increase the tortuosity of irregular circular channels in the porous medium by increasing D_T from 1.1 to 1.26 (Fig. 10b), the permeability values decrease to even lower values. This is also in agreement with the expectations and the physics of flow in porous media. The data presented in Fig. 10b show that the permeability for a gob composed of smaller rock fragments initially is $0.004\,\mathrm{cm}^2$ (4×10^5 Darcy), which decreases to $\sim 0.001\,\mathrm{cm}^2$ (1×10^5 Darcy) when the gob is fully compacted under 19.4 MPa stress. For gobs composed of bigger rock fragments initially (Tests B and D), permeabilities decrease from $0.015\,\mathrm{cm}^2$ (15×10^5 Darcy) to $0.005\,\mathrm{cm}^2$ (5×10^5 Darcy). These values represent an almost 6-fold decrease as compared to the values in Fig. 10.

4.4.4 Predicting Permeabilities for Gobs with Flow Channels in the Shape of Triangle and Ellipse

In a gob environment, flow channels may vary in shape from circular to triangular to elliptical. Equation 20 predicts permeability based on different-shaped channels through the use of a shape factor α, as discussed in Sect. 3.2.1. In this study, we have calculated the gob permeability for equilateral triangle- and ellipse-shaped flow channels as a function of loading. In these calculations, D_T and D_P were 1.1 and 2, respectively. Since both of these shapes are regular 2-D objects filling their area domain completely, their D_P is also 2. Equation 13 and $20\sqrt{3}$ were used in Eq. 20 as shape factors for an ellipse and a triangle, respectively. Figure 11a, b presents the predicted values for these two situations.

Figure 11a, b shows that the permeability decreases about an order of magnitude in the case of triangular pore channels (Fig. 11a) compared to the circular ones (Fig. 9) and about 20 times, when the channels are in the shape of an ellipse with a 5:1 aspect ratio (Fig. 11b). As the aspect ratio is increased to 10:1 (shape factor 126.92) and tortuosity and pore-area fractal dimensions are changed to values in Fig. 10b for more tortuous flow paths and irregularly shaped pores, the permeabilities decrease even more. Permeabilities calculated for this situation are given Fig. 12. This may represent a situation where irregular, slit-like channels are meandering in a fractal fragmented porous medium. This seems to be a closer approximation to a gob where flat sandstone and shale rock blocks are piled (Fig. 1) and are compressed under overburden loading. Calculations show that in a fractal porous medium as the complexity and irregularity of pores increase, the permeabilities decrease accordingly.

4.4.5 Comparison of Fractal Model Prediction with Reported Values and the Predictions of Carman–Kozeny (C–K) and Happel (H) Permeability Equations

There are not any field measurements of permeability of gobs due to their inaccessibility for performing direct measurements. However, there are some reported values calculated based on volumetric strains and geomechanical calculations. For instance, Brunner (1985) used gob permeability values in ventilation network models as $1 \times 10^{-7}\,\mathrm{m}^2$ to $1 \times 10^{-5}\,\mathrm{m}^2$ ($1 \times 10^5 - 1 \times 10^7$ Darcy). Ren et al. (1997) estimated the permeability in the gob to be on the order of $1 \times 10^{-10}\,\mathrm{m}^2$ (1×10^2 Darcy) in the compacted region. Wendt and Balusu (2002) used maximum values around $1 \times 10^{-9}\,\mathrm{m}^2$ (1×10^3 Darcy). Whittles et al. (2006) reported calculated values in the range of $5 \times 10^{-7}\,\mathrm{m}^2$ (5×10^5 Darcy) to $1 \times 10^{-8}\,\mathrm{m}^2$ (1×10^4 Darcy) for a gob. Esterhuizen and Karacan (2007) reported calculated values of $1 \times 10^{-9}\,\mathrm{m}^2$ (1×10^3 Darcy). The differences in permeabilities may be related to different coal-seam geologies, different panel layouts and to differences in caving characteristics. Nevertheless, it should be noted

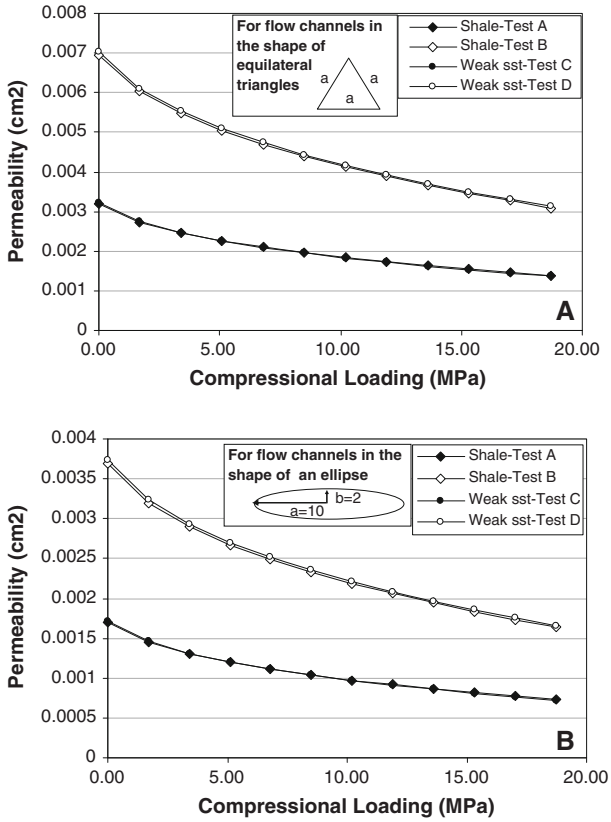

Fig. 11 Predicted permeabilities for a gob simulated in Tests A–D assuming flow channels are in the shape of an equilateral triangle (**a**) and an ellipse (**b**) with 5:1 aspect ratio between its major axes. $D_{\mathrm{T}} = 1.1$ was used as tortuosity

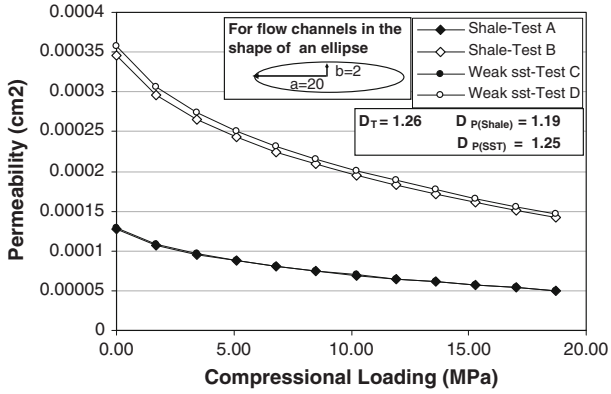

Fig. 12 Predicted permeabilities for gob simulated in Tests A–D assuming flow channels are in the shape of an ellipse with 10:1 aspect ratio between its major axes. $D_{\mathrm{T}} = 1.26$ and D_{P}-values of 1.19 and 1.25 were used for fractal dimensions

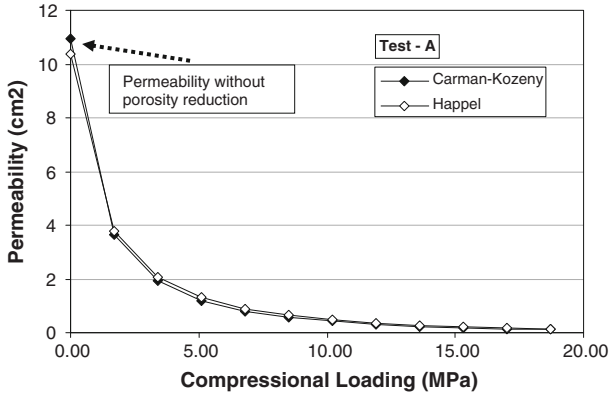

Fig. 13 Predicted permeabilities for gob using Carman–Kozeny and Happel equations (Eqs. 34 and 35)

that all these reported values are within similar orders of magnitude and close to the permeability values calculated by the fractal flow models presented in this study. Thus, the fractal fragmentation and fractal-crushing driven methodologies and the flow models presented in these analyzes predict permeabilities close to the values reported in other studies.

In order to compare the permeability values obtained using the calculation methodology developed in this paper with popular and simpler equations used for flow in aggregates, Carman–Kozeny (C–K) and Happel (H) equations (Li and Logan 2001) presented in Eqs. 34 and 35, respectively, were used. These equations were used to calculate permeability variations only for Test-A. When using these equations, porosity reduction was accounted for as the stress increased and characteristic aggregate size was taken as the average of maximum and minimum particle sizes (33 cm) reported for this test. Figure 13 shows the calculations with C–K and H equations. As this figure indicates, they predict values close to each other. However, these values are orders of magnitude higher than the reported gob permeability values in this and other studies. They are also far from being realistic for a compacted gob. Thus, fractal models developed in this study predict gob permeabilities more realistically than C–K and H equations and thus they are more adequate to use for permeability predictions of a gob environment.

$$k_{\mathrm{C-K}} = \frac{\bar{\Omega}^2}{180} \quad \frac{\phi_T^3}{(1-\phi_T)^2} \tag{34}$$

$$k_H = \frac{\bar{\Omega}^2}{18} \left(\frac{3-4.5\varphi+4.5\varphi^5-3\varphi^6}{\varphi^3(3+2\varphi^5)} \right) \tag{35}$$

where $\varphi = \sqrt[3]{(1-\phi_T)}$

5 Summary and Conclusions

This study developed a predictive approach using the principles of scaling and fractal porous medium combined with fluid flow. This approach allowed the calculation of porosity and permeability from the size distribution of broken rock material in the gob using flow and fractal crushing equations for granular materials. The specific conclusions made from this study can be listed as follows.

(1) Particle size distributions of gob material can be determined from digital pictures or from simulated tests. These data can be used to find the fragmentation fractal dimen-

sion of gob material based on a number–size relationship. This study showed that the number–size relation for different rock materials and gradations can be described with a linear relation. This indicates that the gob material before and after compaction shows fractal scaling properties. Tortuosity and pore-area fractal dimensions can then be determined using the "slit-island" theorem.

(2) Permeability in a fractal porous media can be described using fractal scaling between pore and grain sizes. These information can be used in the Hagen–Poiseuille (H–P) equation to describe flow rate, then which can be integrated with the Darcy equation to describe permeability of a fractal porous media in terms of textural and fractal properties.

(3) Fractal crushing of granular materials can be used in the definition of flow area to simulate compaction of a gob. The porosities predicted using a fractal crushing model were found to be in good agreement with the porosity values calculated using stress–strain data and particle size data. Thus, it is possible using the number–size distribution of a granular media and its fragmentation fractal dimension to calculate changing porosities as stress is progressively increased.

(4) It was observed that the developed fractal model predicts gob permeability at any loading level better than simple models, such as the Carman–Kozeny and Happel equations, since it includes complexities of pores and grains in a completely fragmented porous medium. Predicted permeability values calculated using the fractal permeability model are in better agreement with geomechanical model calculations and reported values in the literature.

(5) It was observed that the size of the rock blocks in the gob make a more dramatic difference in permeability compared to the type of rock material. However, it should also be emphasized that particle size segregation is important as the size distribution controls the fractal properties. Thus, if there is segregation in particle size distribution, at different heights in the gob, this should affect the transport properties of porous medium.

(6) Using the developed approach and the formulations, it is possible change the pore shapes and irregularities determined from gob pictures or to change the tortuosity of flow channels based on expectations to obtain better results. Geometrically, the results showed that circular and smooth channels give the highest permeability. As the irregularity and aspect ratio of the channels increase, permeabilities decrease as expected.

(7) The ultimate benefit of using the approach presented in this paper will be the ability to make better gob reservoir property predictions and to ensure better methane control in the mine environment.

References

Ahmed, A.M.H., Drzymala, J.: Two-dimensional fractal linearization of distributed curves. Physicochem. Probl. Miner. Process. **39**, 129–139 (2005)

Arya, L.M., Paris, J.F.: A physicoemprical model to predict the soil moisture characteristics from particle-size distribution and bulk density data. Soil Sci. Soc. Am. J. **45**, 1023–1030 (1981)

Arya, L.M., Leij, J.F., Van Genucten, M.Th., Shouse, P.: Sealing parameter to predict the soil water characteristics from practicle size distribution data. Soil. Sci. Soc. Am. J. **63**, 510–519 (1999)

Bitelli, M., Gaylon, S.C., Flury, M.: Characterization of particle-size distribution in soils with a fragmentation model. Soil Sci. Soc. Am. J. **63**, 782–787 (1999)

Brunner, D.J.: Ventilation models for longwall leakage simulation. 2nd US Mine Ventilation Symposium, 23–25 September, Reno, NV (1985)

Comegna, V., Damiani, P., Somella, A.: Use of fractal model for determining soil water retention curves. Geoderma **85**, 307–323 (1988)
Esterhuizen, G.S., Karacan, C.Ö.: Development of numerical models to investigate permeability changes and gas emission around longwall mining panels. The AlaskaRocks 2005, 40th US Symposium on Rock Mechanics, Anchorage, Alaska, 25–26 June (2005)
Esterhuizen, G.S., Karacan, C.Ö.: A methodology for determining gob permeability distributions and its application to reservoir modeling of coal mine longwalls. 2007 SME Annual Meeting, Denver, CO (2007)
Griffith, A.A.: The phenomena of rupture and flow in solids. Philos. Trans. R. Soc. Lond. **A221**, 163–198 (1920)
Hunt, A.G., Gee, G.W.: Application of critical path analysis to fractal porous media: comparison with examples from the Hanford site. Adv. Water Resour. **25**, 129–146 (2001)
Jacquin, C.G., Adler, P.M.: Fractal porous media II: geometry of porous geologic structures. Transp. Porous Media **2**, 571–596 (1988)
Karacan, C.Ö., Halleck, P.M.: A fractal model for predicting permeability around perforation tunnels using size distribution of fragmented grains. J. Pet. Sci. Eng. **40**, 159–176 (2003)
Karacan, C.Ö., Esterhuizen, G.S., Schatzel, S.J., Diamond, W.P.: Reservoir simulation-based modeling for characterizing longwall methane emissions and gob gas venthole production. Int. J. Coal Geol. **71**(2–3), 225–245 (2007)
Kozak, E., Pachepsky, Y.A., Sokolowski, S., Sokolowska, Z., Stepniewski, W.: A modified number-based method for estimating fragmentation fractal dimension of soils. Soil Sci. Soc. Am. J **60**, 1291–1297 (1996)
Li, X.-Y., Logan, B.E.: Permeability of fractal aggregates. Water Resour. **35**, 3373–3380 (2001)
Mandelbrot, B.B., Passaja, D.E., Paulley, A.J.: Fractal character of fracture surfaces of metals. Nature **21**, 308 (1994)
McDowell, G.R., Bolton, M.D., Robertson, D.: The fractal crushing of granular materials. J. Mech. Phys. Solids **44**, 2079–2101 (1996)
Mortensen, N.A., Okkels, F., Bruss, H.: Reexamination of Hagen–Poiseuille flow: shape dependence of the hydraulic resistance in microchannels. Phys. Rev. E **71**(057301), 1–4 (2005)
Pappas, D.M., Mark, C.: Behavior of simulated longwall gob material. Report of Investigations RI No. 9458, US Department of Interior, US Bureau of Mines (1993)
Perfect, E.: Fractal models for the fragmentation of rocks and soils: a review. Eng. Geol. **48**, 185–198 (1997)
Perfect, E., Kay, B.D.: Applications of fractals in soil and tillage research: a review. Soil Tillage Res. **36**, 1–20 (1995)
Ren, T.X., Edwards, J.S., Josefowicz, R.R.: CFD modeling of methane flow around longwall coal faces. 6th International Mine Ventilation Congress, 17–22 May, Pittsburgh, PA (1997)
Rieu, M., Sposito, G.: Fractal fragmentation, soil porosity and soil water properties: theory. Soil Sci. Soc. Am. J. **55**, 1231–1238 (1991)
Sammis, C.G., Steacy, S.J. : Fractal fragmentation in crustal shear zones. In: Barton, C., La Pointe, P.R. (eds.) Fractals in the Earth Sciences, pp. 265 Pleanum Publishin Co., New York, NY (1995)
Schlueter, E.M., Zimmerman, R.W., Witherspoon, P.A., Cook, N.G.W.: The fractal dimension of pores in sedimentary rocks and its influence on permeability. Eng. Geol. **48**, 199–215 (1997)
Turcotte, D.L.: Fractals and fragmentation. J. Geophys. Res. **91**, 1921–1926 (1986)
Tyler, S.W., Wheatcraft, S.W.: Application of fractal mathematics to soil water retention estimation. Soil Sci. Soc. Am. J. **53**, 987–996 (1989)
Tyler, S.W., Wheatcraft, S.W.: Fractal scaling of soil particle size distributions: analysis and limitations. Soil Sci. Soc. Am. J. **56**, 363–369 (1992)
Weiss, J.: Fracture and fragmentation of ice: a fractal analysis of scale invariance. Eng. Fract. Mech. **68**, 1975–2012 (2001)
Wendt, M., Balusu, R.: CFD modeling of longwall goaf gas flow dynamics. Coal Saf. **20**, 17–34 (2002)
Wheatcraft, S.W., Tyler, S.W.: An explanation to scale-dependent dispersivity in heterogeneous aquifers using concepts of fractal geometry. Water Resour. Res. **24**, 566–578 (1988)
Whittles, D.N., Lowndes, I.S., Kingman, S.W., Yates, C., Jobling, S.: Influence of geotechnical factors on gas flow experienced in a UK longwall coal mine panel. Int. J. Rock Mech. Min. Sci. **43**, 369–387 (2006)
Yavuz, H.: An estimation of cover pressure re-establishment distance and pressure distribution in the goaf longwall coal mines. Int. J. Rock Mech. Min. Sci. **41**, 193–205 (2004)
Yu, B.M., Cheng, P.: A fractal model for bi-dispersed porous media. Int. J. Heat Mass Transf. **45**(11), 2983–2993 (2002)
Yu, B.M., Liu, W.: Fractal analysis of permeabilities for porous media. AIChE J. **50**(1), 46–57 (2004)